Journal of Applied Polymer Science

WILEY

Applied Polymer Science

RESEARCH ARTICLE OPEN ACCESS

Fundamental Material Parameters Governing the Performance of Polymer-Based Triboelectric Touch Sensors

Maurício M. Kubaski | Nicole R. Demarquette | Ricardo J. Zednik

Department of Mechanical Engineering, École de Technologie Supérieure, Montreal, Canada

Correspondence: Ricardo J. Zednik (ricardo.zednik@etsmtl.ca)

Received: 27 July 2025 | **Revised:** 2 September 2025 | **Accepted:** 17 September 2025

Funding: This work was supported by the Natural Sciences and Engineering Research Council of Canada, RGPIN-2022-05125, Canada Foundation for Innovation, 37555, and Canada Research Chairs Program, 2021-00489.

Keywords: dielectric properties | electrospinning | fibers | sensors and actuators

ABSTRACT

The growing demand for self-powered electronics, such as touch sensors and wearable devices, highlights the need for reliable and efficient triboelectric systems. However, performance inconsistencies frequently originate from uncontrolled material morphology and processing conditions. This study explores the processing–structure–performance relationships in polymer-based triboelectric systems, focusing on poly(vinylidene fluoride) (PVDF). Through controlled experiments incorporating auxiliary materials, poly(3-hydroxybutyrate) (PHB) and carbon nanotubes (CNTs), and characterization via Differential Scanning Calorimetry (DSC), polarized optical microscopy (POM), Fourier transform infrared spectroscopy (FTIR), X-ray diffraction (XRD), and scanning electron microscopy (SEM), we demonstrate that triboelectric performance is primarily driven by crystal size reduction rather than increased crystallinity. Additionally, optimized surface morphology, achieved through electrospinning, significantly enhances output by balancing fiber diameter and defect density. This work establishes a systematic framework for interpreting triboelectric behavior, emphasizes the need for standardization and morphological transparency, and provides guidelines for designing high-performance devices via scalable fabrication methods.

1 | Introduction

Electronics are increasingly small, portable, and versatile, driving a need for compact, low-power sensors for widespread functions like navigation, motion tracking, and environmental monitoring. However, powering these extensive sensor networks solely with batteries presents significant challenges related to cost, maintenance, and environmental impact [1]. To address this, energy-harvesting sensors capable of converting ambient energy into electrical signals are gaining attention.

Self-powered sensing has driven interest in energy-harvesting technologies, with mechanical energy harvesting standing out due to its abundance in daily environments [2–8]. Among these, triboelectric sensors have gained attention for their simplicity, low cost, and efficiency in converting mechanical stimuli into electrical output [3–13]. These devices rely on contact electrification, also known as triboelectricity, which arises from contact or sliding between materials with different surface properties [6, 14–17].

Triboelectric devices can be simply built using a metal and a polymer [18, 19]. Among various polymers, poly(vinylidene fluoride) (PVDF) is particularly promising for triboelectric applications because of its strong electroactive behavior, often attributed to its β-phase conformation, and its high ranking in the triboelectric series [6, 19–22].

Most polymers, including PVDF, are semicrystalline. While the β-phase is frequently associated with enhanced charge

Journal of Applied Polymer Science, 2026; 143:e58025
https://doi.org/10.1002/app.58025

generation in piezoelectric applications [23–33], its role in triboelectric performance remains unclear. The influence of crystalline properties such as crystal size, crystalline phase (e.g., α or β), and degree of crystallinity has not been systematically explored in triboelectric systems.

In addition to crystalline properties, many studies incorporate fillers such as zinc oxide (ZnO), barium titanate ($BaTiO_3$), graphene, or multi-walled carbon nanotubes (CNT) [21, 24, 34–39]. These are typically selected for their dielectric properties or their ability to promote electroactive phases. However, it remains unclear whether the filler addition influences fundamental material behavior or simply varies structural changes.

Surface engineering strategies such as chemical etching, templating, and electrospinning have also been shown to enhance charge generation by increasing surface area and roughness [40–46]. Electrospinning, in particular, enables control over surface morphology, making it a promising technique to tune triboelectric behavior [44]. However, morphological defects such as beads and irregular fibers, which are often overlooked, can significantly reduce charge generation by disrupting uniform charge distribution.

While surface morphology plays a critical role, its effect cannot be fully understood without considering its interaction with the underlying crystalline structure, especially in electroactive polymers like PVDF. Although PVDF's electroactivity is commonly attributed to its β-phase in piezoelectric applications, this relationship may not directly translate to triboelectric systems. A comprehensive understanding requires evaluating the β-phase in conjunction with other structural factors, such as crystal size and surface morphology.

Although interest in triboelectric devices is growing, the relationships between processing, microstructure, and triboelectric performance remain poorly defined. Fillers like CNTs are widely used [47–56], yet their fundamental effects on material structure and electrostatic behavior are often not isolated from changes in morphology or crystallinity. While the triboelectric effect has been known for centuries, its application in energy harvesting and sensing technologies is relatively recent compared to the more established use of piezoelectric devices [57].

This study aims to address these gaps by systematically investigating the effects of crystallinity, crystal size, and surface morphology on the triboelectric response of PVDF in a single-electrode mode device [58]. PVDF samples were processed under controlled conditions to decouple these variables and to isolate the influence of CNT addition.

The results show that crystallinity has minimal impact on output, whereas smaller crystal sizes significantly enhance performance. CNTs contributed only indirectly by acting as nucleating agents. Surface morphology, on the other hand, was capable of altering the triboelectric response by up to an order of magnitude. These findings establish a direct relationship between processing conditions, microstructural features, and triboelectric performance, providing valuable guidance for the development of high-efficiency triboelectric sensors.

2 | Materials and Methods

The study was divided into three main experiments to evaluate the effects of crystalline structure, filler addition, and surface morphology on the generated voltage of a polymer.

The first experiment focused on the influence of crystalline properties. Crystallinity and crystal size were independently varied to assess their individual contributions to triboelectric performance. This was first examined using a model polymer, polyhydroxybutyrate (PHB), processed by compression molding, and subsequently verified for polyvinylidene fluoride (PVDF).

The second experiment investigated the impact of filler addition on generated voltage. Multi-walled carbon nanotubes (CNT) were incorporated into PVDF composites to assess both the intrinsic effect of the filler and its role in further reducing crystal size.

The third experiment explored the influence of surface morphology. Electrospinning was used to fabricate polymer fibers, and solution concentration was systematically varied to tune fiber morphology and evaluate its effect on triboelectric performance.

2.1 | Materials

Pristine PHB was supplied by PHB Industrial under the trade name Biocycle; PVDF was provided by Arkema as Kynar 741. All polymers were used without additives to ensure that intrinsic material properties were isolated. CNTs were provided by Nanocyl under the brand name NC7000. The solvents used for electrospinning were *N*,*N*-dimethylformamide (DMF) supplied by Fisher Chemical, with a purity of 99.8% and acetone from LabChem, with 99.5% purity. For device assembly, conductive copper tape and Kapton film were used as the electrode and substrate, respectively.

2.2 | Experimental

2.2.1 | Compression Molding

Compression molding PHB and PVDF was conducted at 200.0°C under 0.8 MPa for 10.0 min, followed by 10.0 MPa for an additional 10 min. Isothermal crystallization was carried out using two procedures to independently vary crystallinity and crystal size.

To isolate the crystallinity effect on the generated voltage, PHB and PVDF crystal sizes were kept constant by quenching in a 5.0°C ice bath for 30.0 min. Then, they were annealed for different durations as shown in Table 1. To isolate the crystal size effect, PHB and PVDF samples with varying crystal sizes were prepared via isothermal crystallization at varying times and temperatures as shown in Table 2. To keep crystallinity consistent, an annealing step was applied.

The distinct crystal sizes, ranging from the smallest (Figure 1a) to the largest (Figure 1b) for PHB, and similarly for PVDF (Figure 1c,d), were achieved through the isothermal

TABLE 1 | Isothermal crystallization and annealing parameters for evaluating the generated voltage as a function of crystallinity.

Material	Crystallization temperature (°C)	Crystallization duration (min)	Annealing temperature (°C)	Annealing duration (min)
PHB	5.0	30.0	N.A.	N.A.
	5.0	30.0	120.0	0.5
	5.0	30.0	120.0	1.0
	5.0	30.0	120.0	24.0
PVDF	5.0	30.0	N.A.	N.A.
	5.0	30.0	145.0	1.0
	5.0	30.0	145.0	6.0
	5.0	30.0	145.0	24.0

TABLE 2 | Isothermal crystallization and annealing parameters for evaluating the generated voltage as a function of crystal size.

Material	Crystallization temperature (°C)	Crystallization duration (min)	Annealing temperature (°C)	Annealing duration (min)
PHB	5.0	30.0	120.0	24.0
	30.0	30.0	120.0	3.0
	70.0	15.0	120.0	1.0
	90.0	15.0	120.0	0.5
	110.0	45.0	120.0	0.5
	130.0	60.0	120.0	0.5
PVDF	5.0	30.0	145.0	24.0
	30.0	30.0	145.0	12.0
	140.0	30.0	145.0	0.5
	150.0	15.0	145.0	0.5
	150.0	60.0	145.0	0.25
	150.0	120.0	145.0	0.25

crystallization protocols presented in Tables 1 and 2. The smallest and largest crystal size of PHB ranged from 13.0 μm to 8.4 mm. For PVDF, the crystal size ranged from 9.0 to 155.0 μm.

2.2.2 | Carbon Nanotube Dispersion

CNTs were sonicated in acetone for 1 h (Q700, Qsonica, USA, ice bath), then mixed with dissolved PVDF. After solvent evaporation, the solution was adjusted to a 7.0:3.0 (wt./wt.) DMF/acetone ratio, with varying CNT concentrations (0.0–3.0 wt.%). The final mixture (18.0 wt.% PVDF/CNT, 82.0 wt.% solvents) was either dried for compression molding or used for electrospinning.

To evaluate the intrinsic effect of CNT in the generated voltage, the crystal size of the PVDF/CNT composites with different CNT content was quenched to maintain a constant crystal size (approximately 1 μm). To refine the crystalline structure, CNTs were used to promote heterogeneous nucleation and reduce crystal size. PVDF/CNT composites were prepared with varying CNT concentrations and crystallized isothermally at 150.0°C for 120.0 min to promote crystal growth.

2.2.3 | Electrospinning

To investigate the effect of surface morphology on generated voltage, PVDF and PVDF/CNT were electrospun at concentrations listed in Table 3. PVDF was dissolved in a 7.0:3.0 (wt./wt.) DMF/acetone mixture. The PVDF/CNT solution obtained from the previously described dispersion protocol was electrospun as prepared. All solutions were stirred at 60.0°C for 3.0 h and cooled to room temperature before electrospinning.

Electrospinning was performed using a Fluidnatek LE-100 (Bioinicia, Spain) with a 27G needle emitter and a rotating drum collector (1000.0 rpm, 10.5 m/s), covered with parchment paper [59]. Key parameters are listed in Table 3. Nanofibers for device fabrication were carefully detached from the substrate.

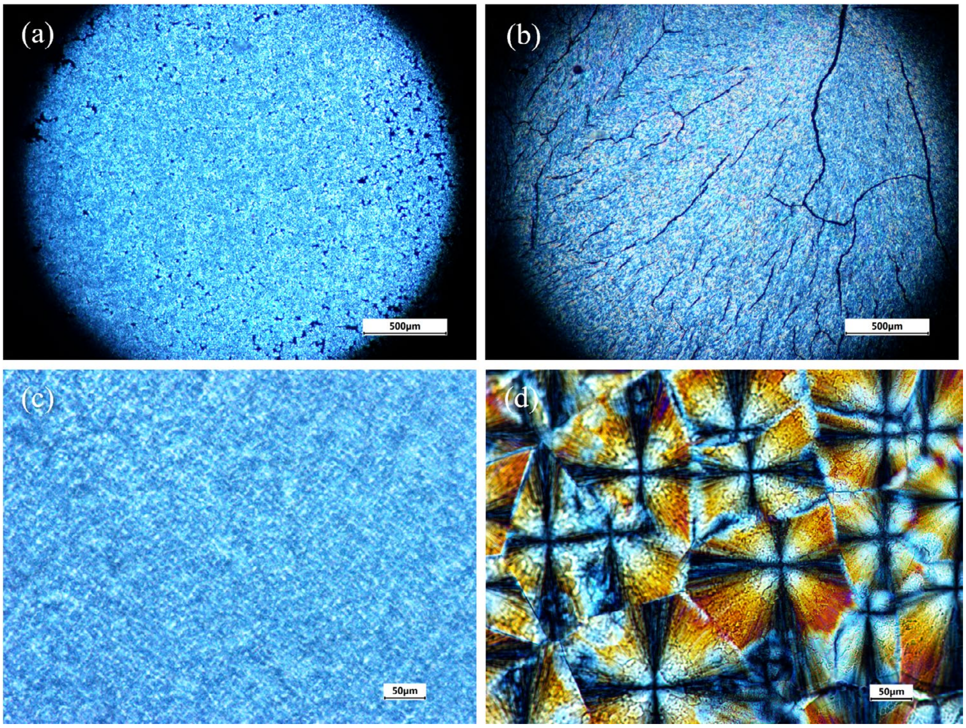

FIGURE 1 | Micrographs showing the effect of varying isothermal crystallization conditions on PHB: (a) 5.0°C, 30.0 min; (b) 130.0°C, 60.0 min; and on PVDF: (c) 5.0°C, 30.0 min; (d) 150.0°C, 120.0 min. [Color figure can be viewed at wileyonlinelibrary.com]

TABLE 3 | Electrospinning parameters for the studied polymers.

Material	Solution concentration (%)	CNT concentration (%)	Applied voltage (kV)	Distance (cm)	Flow rate ($\mu L\,h^{-1}$)	Spinning time (h)
PVDF	10.0, 12.0, 14.0, 16.0, 18.0, 20.0, 22.0, 24.0, and 26.0	0.0	22.0	20.0	1500.0	3.0
PVDF/CNT	18.0	0.0, 0.25, 0.5, 0.75, 1.0, and 3.0	22.0	20.0	1500.0	3.0

Fiber morphology was assessed based on defects and diameter variation. Defects were defined as features exceeding the average fiber diameter, such as oversized fibers or beads. Figure 2 presents a typical image of electrospun fibers obtained from an 18.0 wt.% PVDF solution, with an average diameter of 258.0 nm. We analyzed these images to identify fiber diameters and quantify defects. Defects were defined as fibers with diameters significantly above the average for their respective solution (e.g., 850.0 nm in Figure 2a) and the presence of beads (e.g., 5.1 µm in Figure 2b).

2.2.4 | Triboelectric Device Assembly

Triboelectric devices were assembled in single-electrode mode, where only the bottom electrode is connected to the measuring system [2, 4, 33, 58]. These devices consist of a conductive substrate attached to the electroactive polymer (bottom electrode), while the top electrode may be absent or composed of a metal-coated substrate.

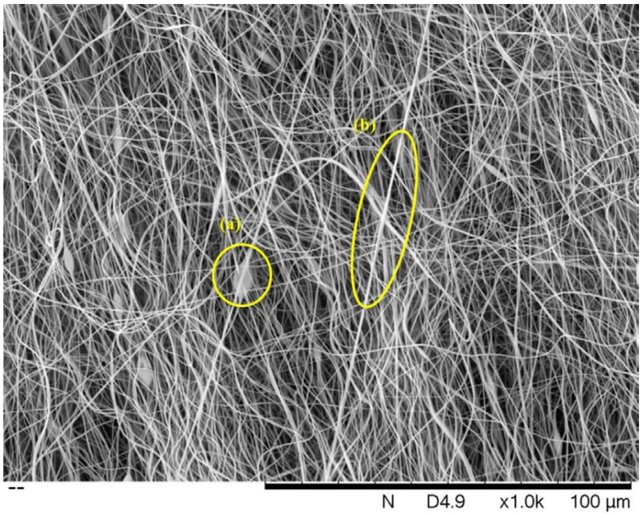

FIGURE 2 | Typical morphologies of bead (a) and large fiber (b). [Color figure can be viewed at wileyonlinelibrary.com]

A schematic design and photograph of the assembly are presented in Figure 3. It consisted of two electrodes: a Kapton film with copper tape (top electrode) and a Kapton film with copper tape, as well as an electroactive material, PHB, PVDF, and PVDF/CNT (bottom electrode). Aluminum wires connected the device to the circuit. The geometry included a 10.0 × 10.0 mm active area, 2.0 mm electrode spacing, and sample thicknesses of 1.0 mm (compression-molded) and 0.1 mm (electrospun).

2.3 | Characterization

2.3.1 | Differential Scanning Calorimetry: Crystallinity

Crystallinity of PHB and PVDF was measured using a DSC 2500 (TA Instruments, Newcastle, DE, USA). The samples were encapsulated in standard aluminum pans and lids. Under nitrogen atmosphere, the samples were heated from 40.0°C to 200.0°C at a rate of 10.0°C min^{-1}. The crystallinity was calculated based on the sample melting enthalpy. Crystallinity [χ_c, Equation (1)] was calculated from the first-heat enthalpy (ΔH_f) using reference values for 100.0% crystalline materials (ΔH_f^*) of: 146.0 J g^{-1} for PHB and 104.5 J g^{-1} for PVDF [60, 61].

$$\chi_c = \frac{\Delta H_f}{\Delta H_f^*} \times 100.0\% \tag{1}$$

2.3.2 | Polarized Optical Microscopy: Crystal Morphology of Compression-Molded Samples

The crystal morphology of the compression-molded samples was analyzed using polarized optical microscopy (POM) with an Olympus BX51 microscope from Olympus Co., Japan, equipped with a hot stage. Crystal sizes were measured using ImageJ software.

2.3.3 | Fourier Transform Infrared Spectroscopy: β-Phase Fraction

Fourier transform infrared spectroscopy (FTIR) was performed on PVDF and PVDF/CNT samples, processed via compression molding and electrospinning, to assess β-phase fraction. Spectra were acquired using a Spectrum Two FTIR spectrometer from PerkinElmer, USA.

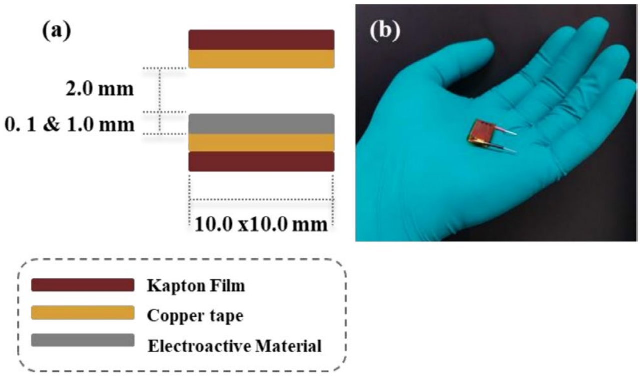

FIGURE 3 | (a) Device schematic; (b) Image of assembled device. [Color figure can be viewed at wileyonlinelibrary.com]

The β-phase fraction $F(\beta)$ (Equation 2) was calculated by comparing the absorption peak intensities at 763.0 cm^{-1} (α-phase, A_α) and 840.0 cm^{-1} (β-phase, A_β), using an absorption coefficient ratio (K_β / K_α) of 1.26 [62].

$$F(\beta) = \frac{A_\beta}{\left(\frac{K_\beta}{K_\alpha}\right) A_\alpha + A_\beta} \tag{2}$$

2.3.4 | X-Ray Diffraction: Crystal Morphology of Electrospun Fibers

X-ray diffraction (XRD) was performed on electrospun fibers to determine crystal size. Measurements were carried out using an XRDynamic 500 diffractometer from Anton Paar, Graz, Austria. Equipped with Cu Kα radiation, a step size of 0.01°, and a 2θ range of 10.0 to 45.0°. The average crystal size (D) was calculated using the Scherrer equation (Equation 3) [63].

$$D = \frac{0.9 \cdot \lambda}{\beta_s \cdot \cos\theta} \tag{3}$$

where D is the average crystal size (nm), λ is the Cu Kα wavelength (1.54 Å), β_s is the full-width at half-maximum (FWHM) in radians, and θ is the Bragg angle in radians.

2.3.5 | Scanning Electron Microscopy: Surface Morphology of Electrospun Fibers

Electrospun fibers morphology was analyzed using scanning electron microscopy (SEM) with a TM3000 microscope from Hitachi, Japan. Samples were gold-coated, mounted on conductive carbon tape, and grounded with copper tape.

Fiber diameters and defect densities were quantified from SEM images using ImageJ software. At least 100 measurements were taken for fiber diameter analysis. Defect density was quantified from SEM micrographs at 1000.0× magnification. An initial control analysis across different regions indicated less than 5% variation in defect counts, so subsequent measurements were taken from a single representative micrograph per sample. Given the constant working distance used, depth-of-field effects were negligible, and all samples were collected after identical electrospinning durations to ensure consistency.

2.3.6 | Oscilloscope: Triboelectric Response

The triboelectric response was measured using an InfiniiVision DSOX3014T oscilloscope (Keysight, USA) with a 1.0 MΩ input impedance. Measurements were conducted in open-circuit mode. A force of 0.2 N was repeatedly applied at 0.5 Hz by dropping a weight from a height of 5.0 cm onto the triboelectric device, inducing contact-separation cycles. This force is above the minimum threshold for human touch detection (> 0.1 N), as reported in previous studies [64–68]. For each sample, at least 10 measurements were done under ambient conditions (21.0°C and 40.0% humidity) and subsequently averaged to determine the triboelectric response.

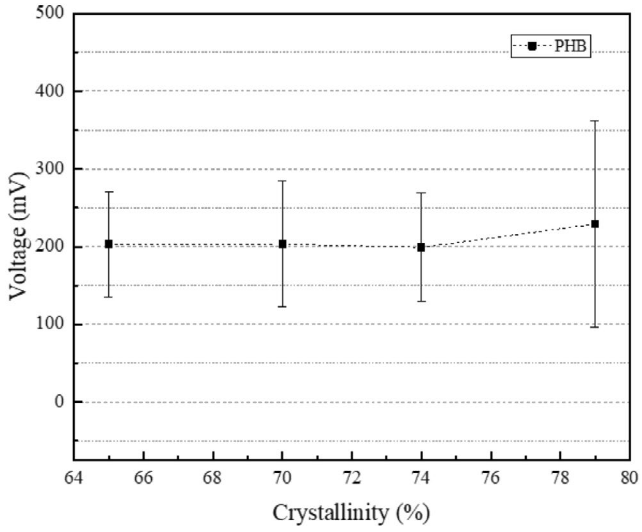

FIGURE 4 | PHB triboelectric response as a function of crystallinity.

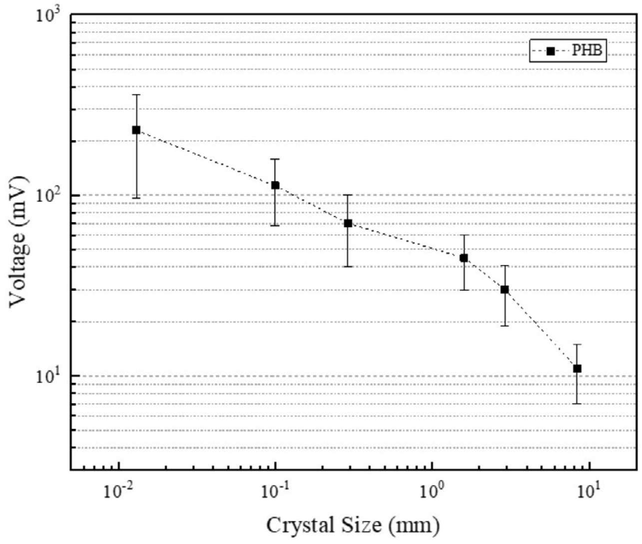

FIGURE 5 | PHB generated voltage as a function of crystal size.

3 | Results and Discussion

It is important to note that all measurements in this study were performed under controlled conditions (21.0°C, 40.0% relative humidity, 0.2 N load). While this approach enabled isolation of crystalline and morphological effects, environmental humidity and repeated cycling are known to significantly influence triboelectric response.

Previous studies have shown that high humidity can reduce charge retention and stability [69, 70]. The present results should therefore be interpreted within the controlled environment used, and future work will systematically examine performance under varying humidity (20%–80%) and long-term cycling to assess sensor durability in practical conditions.

The applied load of 0.2 N is above the typical threshold for human touch (> 0.1 N) [64–68], ensuring that the measurements approximate practical tactile sensing scenarios. While implemented via a controlled weight drop to maintain reproducibility, real finger interactions may involve more complex dynamics, which could be explored in future studies.

3.1 | The Impact of Crystalline Properties in Triboelectric Response

When presenting the triboelectric series, the literature rarely addresses how processing conditions and crystalline properties influence triboelectric response [9, 71–74]. To investigate this, PHB was selected as a model polymer due to its tunable crystalline properties and later compared with PVDF, a common electroactive material.

Figure 4 shows the triboelectric response of PHB as a function of crystallinity, with crystal size held constant at 13.0 μm. No significant change in voltage was observed as crystallinity varied from 65.0% to 79.0%, indicating that crystallinity alone does not influence charge generation when crystal size is fixed.

In contrast, Figure 5 illustrates a strong dependence on crystal size: at constant crystallinity (77.8%), the triboelectric response increased significantly as crystal size decreased, rising from 11.0 mV at 8.4 mm to 229.2 mV at 13.0 μm. This result confirms that crystal size is a key factor in triboelectric performance for PHB.

A similar trend was observed for PVDF. When crystal size (8.2 μm) and β-phase fraction (30.0%) were held constant, variations in crystallinity from 44.0% to 60.5% had minimal impact on the generated voltage. However, reducing crystal size from 155.0 to 9.0 μm, while maintaining constant crystallinity (59.6%) and β-phase fraction (35.7%), led to a fivefold increase in generated voltage (from 34.7 to 171.3 mV). These results further reinforce the conclusion that crystal size, rather than crystallinity, governs triboelectric performance in semicrystalline polymers.

While direct correlations between crystal size and triboelectric response are rare, comparable behavior has been reported in electret studies. For example, smaller crystal sizes in polypropylene enhanced charge retention [74, 75]. This is consistent with theoretical models suggesting that smaller crystals, by introducing more grain boundaries, reduce charge mobility and facilitate interfacial charge trapping [9, 76–78].

3.2 | Influence of CNT Concentration on the Triboelectric Response of PVDF/CNT Composites

Many CNT-based triboelectric devices reported in the literature attribute performance enhancements solely to the presence of CNTs, often without accounting for morphological or structural variations introduced during processing [36, 49, 79, 80]. This makes it difficult to isolate the intrinsic contribution of CNTs to triboelectric behavior.

To address this, CNT concentration was varied while keeping crystal size constant by quenching the samples. As shown in Figure 6a,

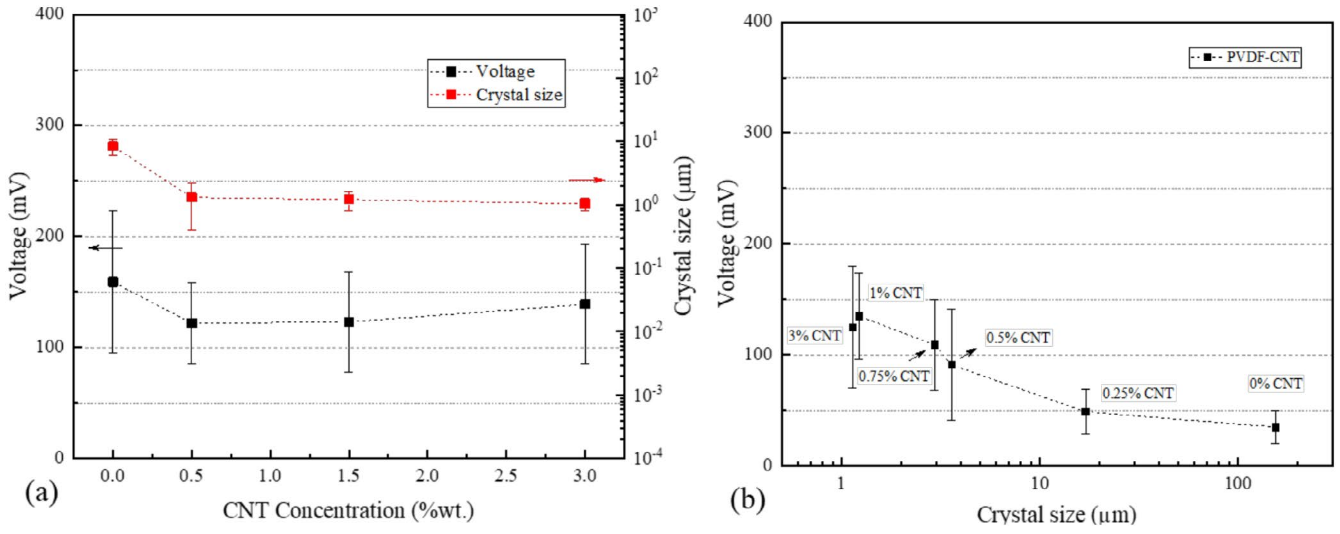

FIGURE 6 | PVDF/CNT generated voltage as a function of (a) CNT concentration; (b) crystal size. [Color figure can be viewed at wileyonlinelibrary.com]

the generated voltage remained nearly constant (136.0 mV), as did the crystal size (1.2 μm), across all CNT concentrations tested. This indicates that CNTs have no direct intrinsic effect on triboelectric performance when surface morphology is controlled.

In contrast, when crystallization happened under favorable conditions (150°C, 120 min), CNTs promoted nucleation and altered the crystalline structure. Figure 6b shows that increasing CNT content from 0.0 to 1.0 wt.% reduced crystal size from 155.0 to 1.2 μm, while the triboelectric response increased from 34.7 to 135.0 mV.

This trend is similar to the behavior observed for both PHB and PVDF, further confirming that the performance enhancement results from crystal size reduction rather than CNT content itself. Beyond 1.0 wt.% CNT, changes in crystal size and generated voltage were minimal, reinforcing the conclusion that CNTs influence triboelectric performance indirectly through nucleation effects.

3.3 | Surface Morphology and Generated Voltage in Electrospun Fibers

Processing conditions, particularly those affecting surface morphology, have a strong influence on triboelectric performance, as highlighted in previous studies where electrospun PVDF/graphene outperformed spin-coated films by over 100% [49, 81, 82]. To further explore this, the effects of defect density and fiber diameter were investigated in electrospun PVDF and PVDF/CNT composites, while controlling for microstructural variables. Crystal size and β-phase fraction were kept constant at 52.5 nm and 82.8%, respectively, across PVDF and PVDF/CNT samples to isolate morphological effects.

As shown in Figure 7, reducing defect density led to a substantial increase in generated voltage. For neat PVDF, voltage increased from 55.3 mV at 10.1×10^3 defects mm^{-2} (10.0 wt.%) to 764.4 mV at 0.4×10^3 defects mm^{-2} (18.0 wt.%), representing a 14-fold enhancement. However, at higher concentrations (20.0–22.0 wt.%), defect density dropped, and the response declined to 147.6 mV. A similar trend was observed in PVDF/CNT composites, where increasing CNT content (0.25–3.0 wt.%) at fixed PVDF concentration (18.0 wt.%) raised defect density and reduced output voltage from 299.0 mV (2.3×10^3 defects mm^{-2}) to 107.9 mV (6.4×10^3 defects mm^{-2}).

As previously shown, the intrinsic effect of CNTs can be decoupled from performance, confirming that the observed trend in Figure 7 arises solely from changes in surface morphology. These results indicate that both systems are highly sensitive to surface defect density, and optimal performance is achieved at intermediate levels where defects are minimized but not entirely eliminated.

Fiber diameter also critically affects performance. As provided in the Supporting Information, Figure S1 shows that for pure PVDF samples, the fiber diameter increases with increasing polymer concentration. In contrast, for the PVDF/CNT composite, fiber diameter decreases as the CNT concentration rises, as shown in Figure S2. This variation, however, is not as significant as that observed for the pure polymer.

Using the same samples analyzed for defect density, Figure 8 shows that generated voltage increased with fiber diameter, peaking at 764.4 mV for 258.0 nm (18.0 wt.%), and then declined to 147.6 mV at 815.0 nm (22.0 wt.%). PVDF/CNT composites followed a similar trend, with a maximum output of 299.0 mV at 155 nm (0.25 wt.% CNT). This behavior suggests an optimal fiber diameter range exists. Within this range, increased surface area enhances charge transfer while minimizing defect-induced charge loss.

A plausible explanation for the peak in triboelectric response at intermediate concentrations relates to the effective crystalline surface available for charge transfer. At low concentrations (10.0 wt.%), the high defect density of 10.1×10^3 defects mm^{-2} limits charge uniformity and reduces the functional crystalline

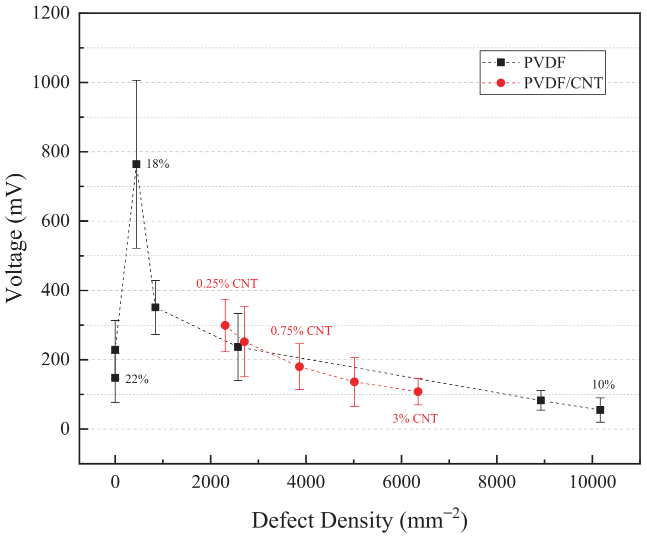

FIGURE 7 | Generated voltage of electrospun PVDF and PVDF/CNT composites as a function of defect density. [Color figure can be viewed at wileyonlinelibrary.com]

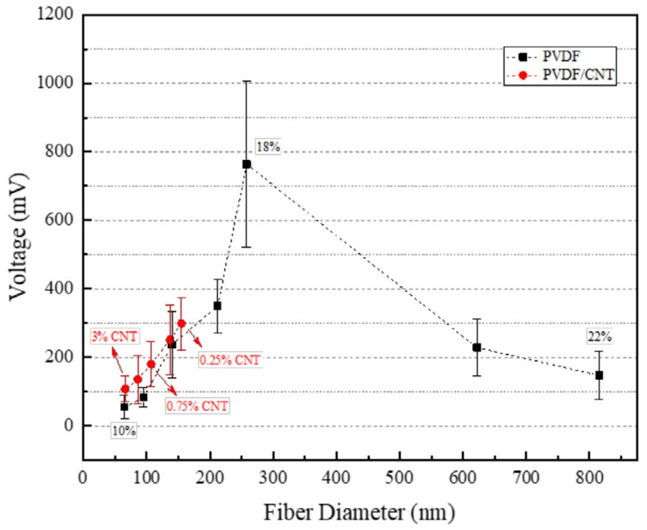

FIGURE 8 | Generated voltage of PVDF and PVDF/CNT composites with increasing fiber diameter. [Color figure can be viewed at wileyonlinelibrary.com]

TABLE 4 | Comparative analysis between existing triboelectric devices.

Material	Generated voltage	Voltage increase	References
Silica gel/silver nanoparticles	From 80.0 to 103.0 V	28.7%	[50]
PVDF/graphene	From 1087.0 to 1511.0 V	39.0%	[49]
PVDF/MoS$_2$	75.0 and 120.0 V	60.0%	[83]
PVDF/graphene oxide	From 140.0 to 450.0 V	221.4%	[53]
P(VDF-TrFE)/BTO	35.0 and 45.0 V	28.6%	[47]
PVDF	From 34.7 to 764.4 mV	2102.9%	This study

area, resulting in a low generated voltage of 55.3 mV. At high concentrations (22.0 wt.%), although defect density decreases to 0.0 defects mm^{-2}, the accompanying increase in fiber diameter to 815.0 nm lowers the total number of fibers per unit area. This reduction in accessible crystalline domains corresponds to a decline in generated voltage to 147.6 mV. The maximum performance is observed at 18.0 wt.% PVDF, where a defect density of 0.4×10^3 defects mm^{-2} and an average fiber diameter of 258.0 nm combine to generate 764.4 mV.

Previous studies have attributed enhanced triboelectric performance to increased β-phase content, particularly in P(VDF-TrFE) copolymers or nanoparticle-modified PVDF composites [47, 49, 52, 53, 83]. However, in those studies, β-phase variations were generally accompanied by changes in morphology or crystal size, making it difficult to isolate their effects. In the present work, the β-phase fraction was intentionally kept constant across processing conditions, allowing the roles of crystal size and morphology to be decoupled. Under these conditions, variations in triboelectric response were independent of β-phase content, highlighting that crystal size and surface morphology are the primary factors influencing response in this system.

Table 4 summarizes studies investigating modifications and their impact on triboelectric performance. The studies were selected based on the relevance of the structural changes examined. Although structural modifications were reported, they were generally not identified as the primary cause of increased generated voltage.

While changes in filler content, filler size, and surface morphology have all been explored in studies presented in Table 4, the trends indicate that surface morphology has the most significant impact on triboelectric performance. In this study, when comparing the two processing techniques, compression molding and electrospinning, the generated voltage ranged from 34.7 to 764.4 mV, corresponding to a 2100% increase. This dramatic enhancement, by more than an order of magnitude, further emphasizes the critical role of surface morphology in controlling triboelectric response.

Together, these results demonstrate that optimal triboelectric response arises from a balance between minimizing defects and maintaining small fiber diameters, conditions that maximize the effective crystalline surface available for charge generation. This confirms that electrospun morphology, rather than filler effects, is the dominant factor controlling device performance.

4 | Conclusions

This study demonstrates that the generated voltage of semicrystalline polymer systems is primarily governed by crystal size and surface morphology, rather than filler content alone. By isolating crystal size and morphology from the influence of the β-phase, we observed that at the β-phase fractions investigated, no direct correlation with triboelectric response was observed. Instead, performance enhancement was dominated by crystal size and morphology. CNTs contributed only indirectly, by promoting nucleation and thereby reducing crystal size.

For the semicrystalline polymers studied, achievable crystallinity was limited to 44.0%–60.5% for PVDF and 65.0%–79.0% for PHB to preserve consistent crystal morphology. The thermal protocols explored this practical range while isolating crystallinity effects from crystal size. These results do not exclude the possibility of different triboelectric behavior at lower crystallinities (<40.0%), which should be investigated in future work.

In electrospun fibers, morphology emerged as a dominant factor. Thin fibers (<200.0 nm) formed at low concentrations exhibited high defect densities ($>0.8\times10^3$ defects mm^{-2} and >500.0 nm), reducing performance. At high concentrations, fibers became too thick (>600.0 nm), also lowering the output despite minimal defects. Optimal generated voltage was achieved at intermediate fiber diameters with low defect density, emphasizing the importance of balancing these parameters.

These results indicate that maximum triboelectric output occurs when the effective crystalline surface available for charge transfer is maximized, which requires simultaneously minimizing surface defects and avoiding excessively large fiber diameters. This highlights that processing-controlled morphology, rather than bulk crystallinity or chemical composition, is the critical determinant of performance.

Overall, these findings highlight the critical role of processing–structure–performance relationships in optimizing triboelectric devices and the limitations of interpreting results based solely on chemical composition or triboelectric series rankings without accounting for microstructural context.

Author Contributions

Maurício M. Kubaski: conceptualization (lead), data curation (lead), formal analysis (equal), investigation (lead), methodology (lead), writing – original draft (lead). **Nicole R. Demarquette:** formal analysis (equal), investigation (equal), methodology (equal), project administration (supporting), resources (lead), supervision (supporting), writing – review and editing (supporting). **Ricardo J. Zednik:** conceptualization (equal), formal analysis (equal), funding acquisition (lead), project administration (lead), resources (lead), supervision (lead), validation (equal), writing – review and editing (supporting).

Acknowledgments

The authors are grateful to Dr. Mazen Samara for his technical assistance. The authors also acknowledge with appreciation the funding provided by the Natural Sciences and Engineering Research Council of Canada (NSERC) Discovery Grant RGPIN-2022-05125, the Canada Foundation for Innovation (CFI) grant 37555, and the Canada Research Chairs Program (CRC) grant 2021-00489.

Conflicts of Interest

The authors declare no conflicts of interest.

Data Availability Statement

The data and experimental results used in this study will be made available by any reasonable request to the corresponding author.

References

1. C. Xu, Y. Song, M. Han, and H. Zhang, "Portable and Wearable Self-Powered Systems Based on Emerging Energy Harvesting Technology," *Microsystems & Nanoengineering* 7, no. 1 (2021): 25, https://doi.org/10.1038/s41378-021-00248-z.

2. W. Akram, Q. Chen, G. Xia, and J. Fang, "A Review of Single Electrode Triboelectric Nanogenerators," *Nano Energy* 106 (2023): 108043, https://doi.org/10.1016/j.nanoen.2022.108043.

3. A. Bindhu, A. P. Arun, and M. Pathak, "Review on Polyvinylidene Fluoride-Based Triboelectric Nanogenerators for Applications in Health Monitoring and Energy Harvesting," *ACS Applied Electronic Materials* 6, no. 1 (2024): 47–72, https://doi.org/10.1021/acsaelm.3c01297.

4. Z. Li, Q. Zheng, Z. L. Wang, and Z. Li, "Nanogenerator-Based Self-Powered Sensors for Wearable and Implantable Electronics," *Research* 2020 (2020): 8710686, https://doi.org/10.34133/2020/8710686.

5. M. Davoudi, C.-Y. An, and D.-E. Kim, "A Review on Triboelectric Nanogenerators, Recent Applications, and Challenges," *International Journal of Precision Engineering and Manufacturing-Green Technology* 11, no. 4 (2024): 1317–1340, https://doi.org/10.1007/s40684-023-00569-6.

6. Z. Khosroshahi, F. Karimzadeh, M. H. Enayati, H. G. B. Gowda, and U. Wallrabe, "Humidity Resistant Triboelectric Nanogenerators for Wind Energy Harvesting: A Review," *Renewable & Sustainable Energy Reviews* 216 (2025): 115650, https://doi.org/10.1016/j.rser.2025.115650.

7. W. Xu, Q. Ren, J. Li, et al., "Triboelectric Contact Localization Electronics: A Systematic Review," *Sensors* 24, no. 2 (2024): 449, https://doi.org/10.3390/s24020449.

8. Y. Liu, J. Wang, T. Liu, et al., "Triboelectric Tactile Sensor for Pressure and Temperature Sensing in High-Temperature Applications," *Nature Communications* 16, no. 1 (2025): 383, https://doi.org/10.1038/s41467-024-55771-0.

9. S. Pan and Z. Zhang, "Fundamental Theories and Basic Principles of Triboelectric Effect: A Review," *Friction* 7, no. 1 (2019): 2–17, https://doi.org/10.1007/s40544-018-0217-7.

10. Z. Ren, L. Wu, Y. Pang, W. Zhang, and R. Yang, "Strategies for Effectively Harvesting Wind Energy Based on Triboelectric Nanogenerators," *Nano Energy* 100 (2022): 107522, https://doi.org/10.1016/j.nanoen.2022.107522.

11. Y. Jiang, X. Liang, T. Jiang, and Z. L. Wang, "Advances in Triboelectric Nanogenerators for Blue Energy Harvesting and Marine Environmental Monitoring," *Engineering* 33 (2024): 204–224, https://doi.org/10.1016/j.eng.2023.05.023.

12. M. A. M. Hasan, W. Zhu, C. R. Bowen, Z. L. Wang, and Y. Yang, "Triboelectric Nanogenerators for Wind Energy Harvesting," *Nature Reviews Electrical Engineering* 1 (2024): 453–465, https://doi.org/10.1038/s44287-024-00061-6.

13. Y. Zhou, P. Lu, X. Zhou, et al., "Triboelectric Wind Sensors: Fundamentals, Progress, and Perspectives," *Nano Energy* 131 (2024): 110209, https://doi.org/10.1016/j.nanoen.2024.110209.

14. D. J. Lacks and R. M. Sankaran, "Contact Electrification of Insulating Materials," *Journal of Physics D: Applied Physics* 44, no. 45 (2011): 453001, https://doi.org/10.1088/0022-3727/44/45/453001.

15. Y. S. Choi, S. Kim, and S. Kar-Narayan, "Materials-Related Strategies for Highly Efficient Triboelectric Energy Generators," *Advanced*

Energy Materials 11, no. 7 (2021): 2003802, https://doi.org/10.1002/aenm.202003802.

16. Y. Nurmakanov, G. Kalimuldina, G. Nauryzbayev, D. Adair, and Z. Bakenov, "Structural and Chemical Modifications Towards High-Performance of Triboelectric Nanogenerators," *Nanoscale Research Letters* 16, no. 1 (2021): 122, https://doi.org/10.1186/s11671-021-03578-z.

17. Y. Lee, S. G. Kang, and J. Jeong, "Sliding Triboelectric Nanogenerator With Staggered Electrodes," *Nano Energy* 86 (2021): 106062, https://doi.org/10.1016/j.nanoen.2021.106062.

18. A. Segkos and C. Tsamis, "Rotating Triboelectric Nanogenerators for Energy Harvesting and Their Applications," *Nanoenergy Advances* 3, no. 3 (2023): 170–219, https://doi.org/10.3390/nanoenergyadv3030010.

19. D. Liu, L. Zhou, S. Cui, et al., "Standardized Measurement of Dielectric Materials' Intrinsic Triboelectric Charge Density Through the Suppression of Air Breakdown," *Nature Communications* 13, no. 1 (2022): 6019, https://doi.org/10.1038/s41467-022-33766-z.

20. M. P. Kim, D.-S. Um, Y.-E. Shin, and H. Ko, "High-Performance Triboelectric Devices via Dielectric Polarization: A Review," *Nanoscale Research Letters* 16, no. 1 (2021): 35, https://doi.org/10.1186/s11671-021-03492-4.

21. C. Shee, S. Banerjee, S. Bairagi, et al., "A Critical Review on Polyvinylidene Fluoride (PVDF)/zinc Oxide (ZnO)-based Piezoelectric and Triboelectric Nanogenerators," *Journal of Physics: Energy* 6, no. 3 (2024): 032001, https://doi.org/10.1088/2515-7655/ad405b.

22. N. Ahbab, S. Naz, T.-B. Xu, and S. Zhang, "A Comprehensive Review of Piezoelectric PVDF Polymer Fabrications and Characteristics," *Micromachines* 16, no. 4 (2025): 386, https://doi.org/10.3390/mi16040386.

23. S. Sandhu, X. Karagiorgis, and R. Dahiya, "P(VDF-TrFE) Nanofibers With Ultrathin MoS$_2$ Nanofillers for Improved Energy Harvesting Efficiency," *IEEE Sensors Letters* 8, no. 6 (2024): 1–4, https://doi.org/10.1109/LSENS.2024.3396751.

24. S. Rana and B. Singh, "rGO-Embedded Polymer Nanocomposite Layer for Improved Performance of Triboelectric Nanogenerator," *Journal of Electronic Materials* 53, no. 11 (2024): 6640–6649, https://doi.org/10.1007/s11664-024-11426-w.

25. S. S. Nardekar, K. Krishnamoorthy, P. Pazhamalai, S. Sahoo, and S. J. Kim, "MoS$_2$ Quantum Sheets–PVDF Nanocomposite Film Based Self-Poled Piezoelectric Nanogenerators and Photovoltaically Self-Charging Power Cell," *Nano Energy* 93 (2022): 106869, https://doi.org/10.1016/j.nanoen.2021.106869.

26. A. Šutka, K. Ma¯lnieks, A. Linarts, P. C. Sherrell, X. Yu, and E. Bilotti, "High-Performance Hybrid Triboelectric Generators Based on an Inversely Polarized Ultrahigh β-Phase PVDF," *ACS Applied Energy Materials* 6, no. 18 (2023): 9300–9306, https://doi.org/10.1021/acsaem.3c01196.

27. A. D. Kumar, N. Arunachalam, and R. Jayaganthan, "Electrical Performance of a Triboelectric Nanogenerator Developed Using Ionic Liquid-Processed Polyvinylidene Fluoride Fabricated Through an Additive Manufacturing Technique," *Nano Energy* 129 (2024): 110055, https://doi.org/10.1016/j.nanoen.2024.110055.

28. I. Aazem, C. Kumar, R. Walden, et al., "Electroactive Phase Dependent Triboelectric Nanogenerator Performance of PVDF–TiO$_2$ Composites," *Energy Advances* 4, no. 5 (2025): 683–698, https://doi.org/10.1039/D4YA00525B.

29. J. S. Andrew and D. R. Clarke, "Effect of Electrospinning on the Ferroelectric Phase Content of Polyvinylidene Difluoride Fibers," *Langmuir* 24, no. 3 (2008): 670–672, https://doi.org/10.1021/la7035407.

30. H. M. Ibrahim and A. Klingner, "A Review on Electrospun Polymeric Nanofibers: Production Parameters and Potential Applications," *Polymer Testing* 90 (2020): 106647, https://doi.org/10.1016/j.polymertesting.2020.106647.

31. D. Ji, Y. Lin, X. Guo, et al., "Electrospinning of Nanofibres," *Nature Reviews Methods Primers* 4, no. 1 (2024): 1, https://doi.org/10.1038/s43586-023-00278-z.

32. Y.-Z. Liu, Q. Zhang, X.-X. Wang, et al., "Review of Electrospinning in the Fabrication of Nanogenerators," *ACS Applied Nano Materials* 7, no. 5 (2024): 4630–4652, https://doi.org/10.1021/acsanm.4c00306.

33. J. P. Lee, J. W. Lee, and J. M. Baik, "The Progress of PVDF as a Functional Material for Triboelectric Nanogenerators and Self-Powered Sensors," *Micromachines* 9, no. 10 (2018): 532, https://doi.org/10.3390/mi9100532.

34. Z. Abbas, M. Anithkumar, A. P. S. Prasanna, N. Hussain, S.-J. Kim, and S. M. Mobin, "Triboelectric Nanogenerators Enhanced by a Metal–Organic Framework for Sustainable Power Generation and Air Mouse Technology," *Journal of Materials Chemistry A* 11, no. 48 (2023): 26531–26542, https://doi.org/10.1039/D3TA05178A.

35. G. S. dos Reis, H. P. de Oliveira, I. C. M. Candido, et al., "Supercapacitors and Triboelectric Nanogenerators Based on Electrodes of Greener Iron Nanoparticles/Carbon Nanotubes Composites," *Scientific Reports* 14, no. 1 (2024): 11555, https://doi.org/10.1038/s41598-024-61173-5.

36. A. Huang, Y. Zhu, S. Peng, B. Tan, and X. Peng, "Improved Energy Harvesting Ability of Single-Layer Binary Fiber Nanocomposite Membrane for Multifunctional Wearable Hybrid Piezoelectric and Triboelectric Nanogenerator and Self-Powered Sensors," *ACS Nano* 18, no. 1 (2024): 691–702, https://doi.org/10.1021/acsnano.3c09043.

37. M. M. Rastegardoost, O. A. Tafreshi, Z. Saadatnia, et al., "Highly Durable Triboelectric Nanogenerators Based on Fibrous Fluoropolymer Composite Mats With Enhanced Mechanical and Dielectric Properties," *Materials Today Energy* 38 (2023): 101431, https://doi.org/10.1016/j.mtener.2023.101431.

38. S. Kim, Y. Song, and M. J. Heller, "Influence of MWCNTs on β-Phase PVDF and Triboelectric Properties," *Journal of Nanomaterials* 2017 (2017): 1–7, https://doi.org/10.1155/2017/2697382.

39. X.-X. Wu, J.-J. Zhang, C.-H. Lee, and M.-F. Lin, "Enhanced Triboelectric Properties of Eu$_2$O$_3$-Doped BaTiO$_3$/PVDF-HFP Nanofibers," *Nanoscale* 15, no. 8 (2023): 3823–3831, https://doi.org/10.1039/D2NR05990H.

40. J. M. Baik and J. P. Lee, "Strategies for Ultrahigh Outputs Generation in Triboelectric Energy Harvesting Technologies: From Fundamentals to Devices," *Science and Technology of Advanced Materials* 20, no. 1 (2019): 927–936, https://doi.org/10.1080/14686996.2019.1655663.

41. W. Kim, T. Okada, H.-W. Park, et al., "Surface Modification of Triboelectric Materials by Neutral Beams," *Journal of Materials Chemistry A* 7, no. 43 (2019): 25066–25077, https://doi.org/10.1039/C9TA09990E.

42. Y. Liu, J. Luo, K. Gao, H. Li, P. He, and W. Zhao, "Triboelectric Nanogenerator With Liquid Metal Electrode Surface Microarray Structure for Self-Powered Bidirectional Sensing and Energy Harvester," *Materials Today Communications* 44 (2025): 112151, https://doi.org/10.1016/j.mtcomm.2025.112151.

43. S. Mishra, P. Supraja, D. Haranath, R. R. Kumar, and S. Pola, "Effect of Surface and Contact Points Modification on the Output Performance of Triboelectric Nanogenerator," *Nano Energy* 104 (2022): 107964, https://doi.org/10.1016/j.nanoen.2022.107964.

44. S.-J. Park, M.-L. Seol, S.-B. Jeon, D. Kim, D. Lee, and Y.-K. Choi, "Surface Engineering of Triboelectric Nanogenerator With an Electrodeposited Gold Nanoflower Structure," *Scientific Reports* 5, no. 1 (2015): 13866, https://doi.org/10.1038/srep13866.

45. W. Yang, X. Wang, H. Li, et al., "Fundamental Research on the Effective Contact Area of Micro–/Nano-Textured Surface in Triboelectric Nanogenerator," *Nano Energy* 57 (2019): 41–47, https://doi.org/10.1016/j.nanoen.2018.12.029.

46. G. Zhu, W. Q. Yang, T. Zhang, et al., "Self-Powered, Ultrasensitive, Flexible Tactile Sensors Based on Contact Electrification," *Nano Letters* 14, no. 6 (2014): 3208–3213, https://doi.org/10.1021/nl5005652.

47. H. Yang, J. Wang, Z. Yang, Z. Zhang, J. Wu, and J. Wang, “Enhancement of Triboelectricity Based on Fully Organic Composite Films With a Conducting Polymer,” *ACS Nano* 14, no. 5 (2020): 5898–5906, https://doi.org/10.1021/acsnano.0c01865.

48. M. Ahmed, M. Akhtar, M. M. Islam, et al., “Highly Flexible, Bio-Degradable, and High-Performance Bioplastic-Based Triboelectric Nanogenerators From Cellulose,” *Energy Technology* 12, no. 4 (2024): 2301282, https://doi.org/10.1002/ente.202301282.

49. L. Shi, H. Jin, S. Dong, et al., “High-Performance Triboelectric Nanogenerator Based on Electrospun PVDF-Graphene Nanosheet Composite Nanofibers for Energy Harvesting,” *Nano Energy* 80 (2021): 105599, https://doi.org/10.1016/j.nanoen.2020.105599.

50. M. Ahmed, M. Akhtar, M. M. Islam, et al., “High-Performance Flexible and Biodegradable Triboelectric Nanogenerator Based on Paper and PVA–Borax Hydrogel,” *Nanotechnology* 33, no. 47 (2022): 475402, https://doi.org/10.1088/1361-6528/ac8aa2.

51. H. Su, J. Zheng, L. Tang, et al., “One-Step Electrospinning Synthesis of Lead-Free Perovskite Nanofiber-Based Triboelectric Nanogenerator for Wearable Intelligent Fall Alarm,” *Journal of Colloid and Interface Science* 696 (2025): 137836, https://doi.org/10.1016/j.jcis.2025.137836.

52. H. M. Venkatesan and A. P. Arun, “High-Performance Triboelectric Nanogenerators Based on ag-Doped ZnO Loaded Electrospun PVDF Nanofiber Mats for Energy Harvesting and Healthcare Monitoring,” *Scientific Reports* 15, no. 1 (2025): 3347, https://doi.org/10.1038/s41598-025-87148-8.

53. Y. Dai, X. Zhong, T. Xu, Y. Li, Y. Xiong, and S. Zhang, “High-Performance Triboelectric Nanogenerator Based on Electrospun Polyvinylidene Fluoride–Graphene Oxide Nanosheet Composite Nanofibers,” *Energy Technology* 11, no. 9 (2023): 2300426, https://doi.org/10.1002/ente.202300426.

54. S. Sukumaran, P. K. Szewczyk, T. Bajda, and U. Stachewicz, “Hybrid Piezo-, Pyro-, and Triboelectric Nanogenerator Based on PVDF and rGO Composite Fibers for a Multifunctional Approach to Energy Harvesting Applications,” *Materials & Design* 254 (2025): 114105, https://doi.org/10.1016/j.matdes.2025.114105.

55. S. Qin, P. Yang, Z. Liu, et al., “Triboelectric Sensor With Ultra-Wide Linear Range Based on Water-Containing Elastomer and Ion-Rich Interface,” *Nature Communications* 15, no. 1 (2024): 10640, https://doi.org/10.1038/s41467-024-54980-x.

56. N. Li, P. Yang, Z. Bai, et al., “Bioinspired Electrostatic Capture-and-Release System for Precise Microdroplet Manipulation,” *Advanced Materials* 37, no. 9 (2025): e2418711, https://doi.org/10.1002/adma.202418711.

57. F.-R. Fan, Z.-Q. Tian, and Z. L. Wang, “Flexible Triboelectric Generator,” *Nano Energy* 1, no. 2 (2012): 328–334, https://doi.org/10.1016/j.nanoen.2012.01.004.

58. Z. L. Wang, L. Lin, J. Chen, S. Niu, and Y. Zi, “Triboelectric Nanogenerator: Single-Electrode Mode,” in *Triboelectric Nanogenerators* (Springer, 2016), 91–107.

59. T. Kozior, A. Mamun, M. Trabelsi, M. Wortmann, S. Lilia, and A. Ehrmann, “Electrospinning on 3D Printed Polymers for Mechanically Stabilized Filter Composites,” *Polymers* 11, no. 12 (2019): 2034, https://doi.org/10.1109/NAP.2018.8914823.

60. I. Chiulan, D. M. Panaitescu, A. N. Frone, et al., “Biocompatible Polyhydroxyalkanoates/Bacterial Cellulose Composites: Preparation, Characterization, and in Vitro Evaluation,” *Journal of Biomedical Materials Research, Part A* 104, no. 10 (2016): 2576–2584, https://doi.org/10.1002/jbm.a.35800.

61. J. Liu, X. Lu, and C. Wu, “Effect of Preparation Methods on Crystallization Behavior and Tensile Strength of Poly(Vinylidene Fluoride) Membranes,” *Membranes* 3, no. 4 (2013): 389–405, https://doi.org/10.3390/membranes3040389.

62. X. Cai, T. Lei, D. Sun, and L. Lin, “A Critical Analysis of the α, β and γ Phases in Poly(Vinylidene Fluoride) Using FTIR,” *RSC Advances* 7, no. 25 (2017): 15382–15389, https://doi.org/10.1039/C7RA01267E.

63. V. Savikhin and M. F. Toney, “Organic Thin-Film Microstructure Characterization: Coherence Length,” in *Handbook of Organic Materials for Electronic and Photonic Devices*, 2nd ed., ed. C. C. Ostroverkhova (Woodhead Publishing, 2019), 520–521.

64. S. Logozzo, M. C. Valigi, and M. Malvezzi, “Modelling the Human Touch: A Basic Study for Haptic Technology,” *Tribology International* 166 (2022): 107352, https://doi.org/10.1016/j.triboint.2021.107352.

65. L. Li, T. Xu, M. Xue, et al., “Learning the Human Perceptions of Touch Force Positing and Object Shape Using a Soft Optical Fiber Tactile Sensing Pad,” *Optics and Laser Technology* 179 (2024): 111272, https://doi.org/10.1016/j.optlastec.2024.111272.

66. M. Paré, H. Carnahan, and A. Smith, “Magnitude Estimation of Tangential Force Applied to the Fingerpad,” *Experimental Brain Research* 142, no. 3 (2002): 342–348, https://doi.org/10.1007/s00221-001-0939-y.

67. J. W. Bisley, A. W. Goodwin, and H. E. Wheat, “Slowly Adapting Type I Afferents From the Sides and End of the Finger Respond to Stimuli on the Center of the Fingerpad,” *Journal of Neurophysiology* 84, no. 1 (2000): 57–64, https://doi.org/10.1152/jn.2000.84.1.57.

68. Y. Liu, J. Tao, Y. Mo, R. Bao, and C. Pan, “Ultrasensitive Touch Sensor for Simultaneous Tactile and Slip Sensing,” *Advanced Materials* 36, no. 21 (2024): e2313857, https://doi.org/10.1002/adma.202313857.

69. V. U. Somkuwar, H. Garg, S. K. Maurya, and B. Kumar, “Influence of Relative Humidity and Temperature on the Performance of Knitted Textile Triboelectric Nanogenerator,” *ACS Applied Electronic Materials* 6, no. 2 (2024): 931–939, https://doi.org/10.1021/acsaelm.3c01442.

70. J. Zhang, C. Boyer, and Y. X. Zhang, “Enhancing the Humidity Resistance of Triboelectric Nanogenerators: A Review,” *Small* 20 (2024): e2401846, https://doi.org/10.1002/smll.202401846.

71. Y. Liu, J. Mo, Q. Fu, et al., “Enhancement of Triboelectric Charge Density by Chemical Functionalization,” *Advanced Functional Materials* 30, no. 50 (2020): 2004714, https://doi.org/10.1002/adfm.202004714.

72. Z. Liu, S. Ramakrishna, I. Ahmed, C. Rudd, and X. Liu, “Rheological, Surface Tension and Conductivity Insights on the Electrospinnability of Poly(Lactic-Co-Glycolic Acid)-hyaluronic Acid Solutions and Their Correlations With the Nanofiber Morphological Characteristics,” *Polymers* 14, no. 20 (2022): 4411, https://doi.org/10.3390/polym14204411.

73. J. He, Z. Xie, K. Yao, et al., “Trampoline-Inspired Stretchable Triboelectric Nanogenerators as Tactile Sensors for Epidermal Electronics,” *Nano Energy* 81 (2021): 105590, https://doi.org/10.1016/j.nanoen.2020.105590.

74. A. Thyssen, K. Almdal, and E. V. Thomsen, “Electret Stability Related to Spherulites in Polypropylene,” *IEEE Transactions on Dielectrics and Electrical Insulation* 22, no. 5 (2015): 2858–2863, https://doi.org/10.1109/TDEI.2015.004891.

75. R. R. Xu, B. X. Du, M. Xiao, et al., “Dielectric Properties Dependent on Crystalline Morphology of PP Film for HVDC Capacitors Application,” *Polymer* 213 (2021): 123204, https://doi.org/10.1016/j.polymer.2020.123204.

76. A. K. Hailey, S. Wang, Y. Chen, et al., “Quantifying the Energy Barriers and Elucidating the Charge Transport Mechanisms Across Interspherulite Boundaries in Solution-Processed Organic Semiconductor Thin Films,” *Advanced Functional Materials* 25, no. 35 (2015): 5662–5668, https://doi.org/10.1002/adfm.201501666.

77. H. F. Haneef, A. M. Zeidell, and O. D. Jurchescu, “Charge Carrier Traps in Organic Semiconductors: A Review on the Underlying Physics and Impact on Electronic Devices,” *Journal of Materials Chemistry C* 8, no. 3 (2020): 759–787, https://doi.org/10.1039/C9TC05695E.

78. J. Gao, Q. Jiang, Z. Yao, and H. Ju, “Effect of β-Nucleating Agents on the Crystallization Behavior and Force-Electric Properties of the Polypropylene Blends,” *Journal of Vinyl and Additive Technology* 30, no. 1 (2024): 217–229, https://doi.org/10.1002/vnl.22043.

79. H.-T. Deng, X.-R. Zhang, Z.-Y. Wang, et al., “Super-Stretchable Multi-Sensing Triboelectric Nanogenerator Based on Liquid Conductive Composite,” *Nano Energy* 83 (2021): 105823, https://doi.org/10.1016/j.nanoen.2021.105823.

80. P. Liu, N. Sun, Y. Mi, et al., “Ultra-Low CNTs Filled High-Performance Fast Self-Healing Triboelectric Nanogenerators for Wearable Electronics,” *Composites Science and Technology* 208 (2021): 108733, https://doi.org/10.1016/j.compscitech.2021.108733.

81. Y. Zou, J. Xu, K. Chen, and J. Chen, “Advances in Nanostructures for High-Performance Triboelectric Nanogenerators,” *Advanced Materials Technologies* 6, no. 3 (2021): 2000916, https://doi.org/10.1002/admt.202000916.

82. J. Kočí, M. M. Havlík, V. Procházka, N. Klusoňová, and E. Sedláčková, “The Effect of Solution Viscosity on the Quality of Electroactive Nanofibers Produced by Electrospinning,” *Monatshefte für Chemie-Chemical Monthly* 155, no. 3–4 (2024): 349–352, https://doi.org/10.1007/s00706-023-03156-2.

83. B. Hedau, B.-C. Kang, and T.-J. Ha, “Enhanced Triboelectric Effects of Self-Poled MoS_2-Embedded PVDF Hybrid Nanocomposite Films for Bar-Printed Wearable Triboelectric Nanogenerators,” *ACS Nano* 16, no. 11 (2022): 18355–18365.

Supporting Information

Additional supporting information can be found online in the Supporting Information section. **Data S1:** Supporting Information.